

000 001 002 003 004 005 006 007 008 009 010 011 012 013 014 015 016 017 018 019 020 021 022 023 024 025 026 027 028 029 030 031 032 033 034 035 036 037 038 039 040 041 042 043 044 045 046 047 048 049 050 051 052 053 LLAVA-RADZ: CAN MULTIMODAL LARGE LAN- GUAGE MODELS EFFECTIVELY TACKLE ZERO-SHOT RADIOLOGY RECOGNITION?

006
007 **Anonymous authors**
008 Paper under double-blind review

011 ABSTRACT

013 Recently, Multimodal Large Language Models (MLLMs) have demonstrated ex-
014 ceptional capabilities in visual understanding and reasoning across various vision-
015 language tasks. However, we found that MLLMs cannot process effectively from
016 fine-grained medical image data in the traditional Visual Question Answering
017 (VQA) pipeline, as they do not exploit the captured features and available medical
018 knowledge fully, results in MLLMs usually performing poorly in zero-shot medical
019 disease recognition. Fortunately, this limitation does not indicate that MLLMs
020 are fundamentally incapable of addressing fine-grained recognition tasks. From
021 a feature representation perspective, MLLMs demonstrate considerable potential
022 for tackling such challenging problems. Thus, to address this challenge, we pro-
023 pose **LLaVA-RadZ**, a simple yet effective framework for zero-shot medical dis-
024 ease recognition via utilizing the existing MLLM features. Specifically, we design
025 an end-to-end training strategy, termed *Decoding-Side Feature Alignment Train-
026 ing (DFAT)* to take advantage of the characteristics of the MLLM decoder archi-
027 tecture and incorporate modality-specific tokens tailored for different modalities.
028 Additionally, we introduce a *Domain Knowledge Anchoring Module (DKAM)* to
029 exploit the intrinsic medical knowledge of large models, which mitigates the *cat-
030 egory semantic gap* in image-text alignment. Extensive experiments demonstrate
031 that our LLaVA-RadZ significantly outperforms traditional MLLMs in zero-shot
032 disease recognition, achieving the comparable performance to the well-established
033 and highly-optimized CLIP-based approaches.

034 1 INTRODUCTION

035 With the rapid advancement of deep learning technologies, an increasing number of studies have
036 focused on their applications in medical disease diagnosis, yielding remarkable results (Chan et al.,
037 2020; Jamshidi et al., 2020; Lee et al., 2022; Tran et al., 2021). However, these approaches typi-
038 cally rely on high-quality annotations provided by clinical experts. Unlike natural image datasets,
039 annotating medical images is both costly and time-consuming. To address this challenge, recent
040 research has explored methods based on paired medical images and textual reports, leveraging con-
041 trastive learning techniques. By minimizing the distance between paired samples while maximizing
042 the distance between unpaired ones, these CLIP-based approaches enable zero-shot disease recog-
043 nition, thereby reducing reliance on extensive medical data annotation to a certain extent. In our
044 in-depth investigation of advanced zero-shot disease recognition methods in the medical domain,
045 several representative CLIP-based models (Lai et al., 2024; Wu et al., 2023; Zhang et al., 2023b;
046 Phan et al., 2024) have achieved significant performance improvements leveraging the capabilities
047 of Large Language Models (LLMs) or incorporate expert domain knowledge to some extent, rather
048 than fully leveraging the models' intrinsic understanding capabilities.

049 Recently, Multimodal Large Language Models (MLLMs) (Achiam et al., 2023; Team et al., 2023;
050 Liu et al., 2023; Huang et al., 2024; 2025; You et al., 2025) have demonstrated remarkable capabili-
051 ties across various user-oriented vision-language tasks, such as image comprehension and reasoning,
052 offering new possibilities for zero-shot disease recognition in medical applications. Among these,
053 LLaVA-Med (Li et al., 2024a) has exhibited exceptional domain-specific medical knowledge in
dialogue-based tasks, indicating that it possesses a certain degree of medical expertise. However,

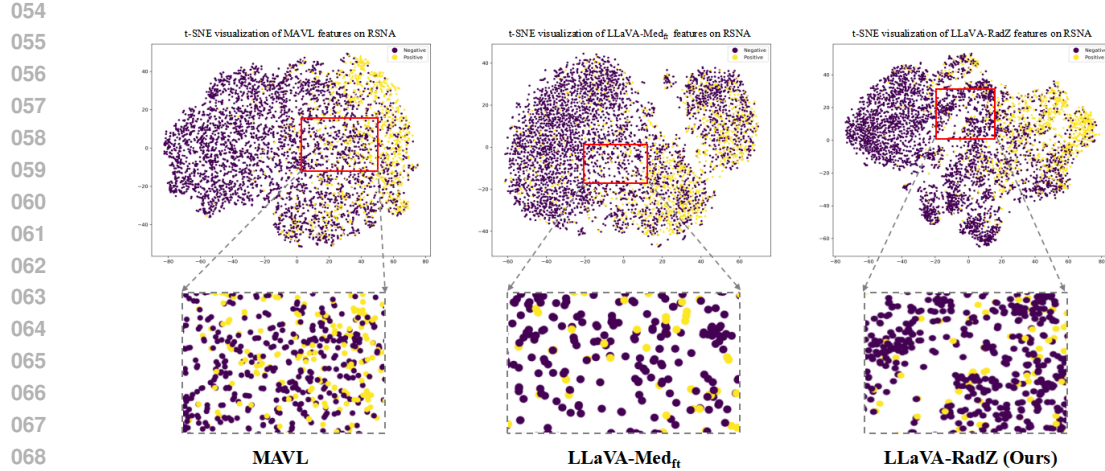


Figure 1: Comparison of Feature Distributions among MAVL, LLaVA-Med_{ft}, and LLaVA-RadZ on the RSNA Dataset.

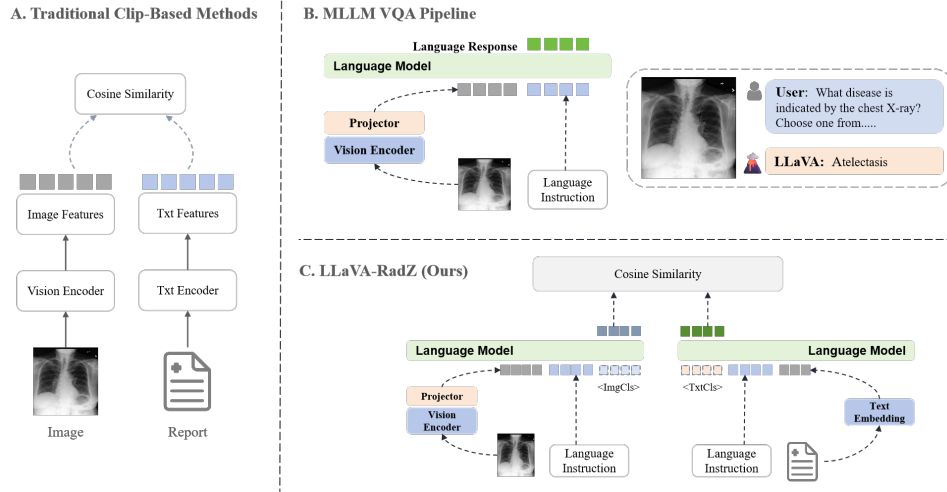


Figure 2: Framework comparison of traditional CLIP-based methods, MLLM VQA pipeline, and the proposed LLaVA-RadZ.

a recent study (Zhang et al., 2024) found that MLLMs, *i.e.*, LLaVA (Liu et al., 2023) performed significantly worse than CLIP (Radford et al., 2021) on standard image classification tasks.

To further validate this observation, we conducted zero-shot classification experiments using multiple MLLMs on five medical imaging datasets (see Tab. 1). The experimental results are consistent with previous findings, confirming that MLLMs exhibit suboptimal performance in image classification, particularly when dealing with complex medical images. To enhance the generalization capability of MLLMs in radiology disease recognition tasks, we employed a fine-tuning strategy and performed supervised fine-tuning on the MIMIC-CXR dataset (Johnson et al., 2019). Additionally, inspired by the work of (Zhang et al., 2024), we incorporated a series of optimizations. While these improvements yielded performance gains, the results remained inferior compared to CLIP-based models. This phenomenon raises a critical question: *Can MLLMs effectively perform zero-shot disease recognition?*

As shown in Fig. 1, we visualize the feature distributions of MAVL (Phan et al., 2024), LLaVA-Med \mathbf{ft} (fine-tuned by the same dataset of our LLaVA-RadZ) and LLaVA-RadZ on the RSNA (Shih et al., 2019) dataset. The results indicate that MLLM exhibits strong feature extraction capabilities, comparable to the well-established MAVL in the domain. However, in the disease recognition task, MAVL significantly outperforms fine-tuned LLaVA-Med. We hypothesize that this performance gap

108 arises because MLLMs fail to fully utilize the extracted features for effective disease identification
 109 via traditional VQA pipeline.
 110

111 Inspired by this, we propose a simple yet effective LLaVA-RadZ framework for zero-shot disease
 112 recognition using the MLLM features. Our proposed framework has the fundamental difference
 113 compared with previous CLIP-base methods and traditional MLLM VQA pipeline. As shown in
 114 Fig. 2, we design a dedicated MLLM feature-based framework to address zero-shot medical disease
 115 recognition. Our proposed framework effectively leverages pre-trained MLLM representations to
 116 overcome the inherent limitations of the traditional VQA pipeline on this task. Specifically, firstly,
 117 we introduce a new training strategy, Decoding-Side Feature Alignment Training (DFAT). Specif-
 118 ically, we introduce special tokens for both image and text modalities and leverage the autoregres-
 119 sive generation capability of the decoder architecture to extract global representations of images and
 120 texts. Additionally, we incorporate a cross-modal contrastive loss to optimize the model’s ability
 121 to learn discriminative features. Furthermore, to mitigate the semantic category gap encountered
 122 during fine-grained alignment between medical images and textual reports, we design a Domain
 123 Knowledge Anchoring Module (DKAM). DKAM utilizes the model’s intrinsic medical knowledge
 124 to extract the semantic information underlying disease categories, constructing disease description
 125 vectors that serve as an intermediary bridge to facilitate the alignment between medical images and
 126 textual reports, thereby establishing a stable relationship. To further enhance the correlation among
 127 medical images, textual reports, and disease categories, a category knowledge-guided loss strength-
 128 ens the association between similar images and corresponding textual reports.
 129

130 Our main contributions can be summarized as follows.
 131

- 132 • We analyze the limitations of current MLLMs in addressing complex fine-grained medical
 133 disease recognition tasks, investigate the underlying causes of these constraints, and pro-
 134 pose a novel end-to-end feature-based MLLM framework to mitigate these challenges. To
 135 the best of our knowledge, we are the *first* work in the field of medical disease recognition
 136 to explore how to use MLLM features directly to solve complex recognition problems.
 137
- 138 • We propose the tailored training strategy DFAT, and incorporate a cross-modal contrastive
 139 loss to optimize the model’s ability to achieve effective alignment between visual and tex-
 140 tual features. Furthermore, we design a DKAM to leverage MLLM’s intrinsic medical
 141 knowledge and effectively mitigate semantic gap in image-text alignment, thereby enhanc-
 142 ing category-level alignment.
 143
- 144 • We conduct extensive experiments on multiple large-scale radiology diagnosis datasets,
 145 validating the potential of LLaVA-RadZ in zero-shot disease recognition tasks.
 146

147 2 APPROACH

148 2.1 CAN MED-LLMs BE GOOD MEDICAL CLASSIFIERS?

149 Previous studies have explored the classification capabilities of multimodal large language models
 150 (MLLMs), revealing that their performance on image classification tasks is often limited. For exam-
 151 ple, (Zhang et al., 2024) investigates the performance differences in classification between MLLMs
 152 and CLIP, focusing on factors such as inference strategies, training approaches, and datasets. In-
 153 spired by this work, we extend the exploration to zero-shot tasks in the medical domain. Unlike
 154 natural images and text, the relationship between medical images and reports is more complex.
 We seek to investigate whether large medical models, leveraging domain-specific knowledge, can
 achieve superior performance on medical zero-shot tasks.
 155

156 We first evaluated two open-source MLLMs, i.e., LLaVA-1.5 (Liu et al., 2023) and LLaVA-Med (Li
 157 et al., 2024a), on five medical datasets in a zero-shot classification setting. The evaluation followed
 158 a general large-model classification approach, where the model selects the correct category from
 159 a set of candidate options. As shown in Tab. 1, these models demonstrated limited performance
 160 in disease classification tasks and failed to accurately identify various medical conditions. Given
 161 the potential knowledge limitations of these models, we further assessed the performance of more
 162 powerful proprietary MLLMs (i.e., Qwen2.5-Max (Yang et al., 2024), Gemini-Pro (Team et al.,
 163 2023), and GPT-4o (Achiam et al., 2023)) on zero-shot medical disease recognition tasks. As shown
 164

162 in table 1, these models exhibited superior classification capabilities. However, they still lagged
 163 behind the state-of-the-art domain-specific methods in medical classification.

164
 165 To enhance the generalization ability of MLLMs in radiology disease identification, we conducted
 166 Supervised Fine-Tuning (SFT) on LLaVA-1.5 (Liu et al., 2023) and LLaVA-Med (Li et al., 2024a)
 167 using the publicly available MIMIC-CXR dataset (Johnson et al., 2019). Surprisingly, the fine-tuned
 168 models did not achieve consistent performance improvements across the five datasets. In some
 169 cases, their classification performance even deteriorated. Further analysis of the model outputs
 170 revealed that MLLMs did not always focus on disease-specific information in radiology reports.
 171 Instead, they tended to overlearn the textual structures and linguistic patterns of the reports, which
 172 limited their classification capability. To mitigate this issue, we incorporated the Chain-of-Thought
 173 (CoT) prompting strategy and adjusted the model’s reasoning approach, inspired by the methodology
 174 of (Zhang et al., 2024), to optimize the model’s decision-making process. This approach led to
 175 moderate improvements in classification performance on medical datasets. Although the models
 176 have not yet reached optimal performance, the results suggest that MLLMs still hold significant
 177 potential for zero-shot medical disease recognition.

178 2.2 MOTIVATION

179 As previously discussed, despite possessing a certain level of domain knowledge, medical MLLMs
 180 have not yet demonstrated remarkable performance in zero-shot medical tasks. Even with further
 181 instruction tuning, their performance remains inferior to that of existing vision-language models
 182 (VLMs). However, it is noteworthy that modifying the inference strategy leads to significant perfor-
 183 mance improvements, suggesting that MLLMs are indeed capable of capturing medical image and
 184 text features. Nevertheless, these features have yet to be fully exploited.

185 To address this limitation, we propose the LLaVA-RadZ framework, introducing a novel end-to-end
 186 training strategy, Decoding-Side Feature Alignment Training (DFAT). This approach leverages the
 187 unique properties of the MLLM decoder architecture while incorporating modality-specific special
 188 tokens to facilitate effective interaction between medical images and textual features, ultimately
 189 achieving more robust cross-modal alignment. As illustrated in Fig. 1, we compare the feature dis-
 190 tribution of our model with MAVL (Pham et al., 2024), the current state-of-the-art method, on the
 191 RSNA (Shih et al., 2019) dataset. The results clearly demonstrate that our model achieves better
 192 clustering of intra-class samples while enhancing inter-class separation, validating the effectiveness
 193 of our approach. Furthermore, we introduce the Domain Knowledge Anchor Module (DKAM),
 194 which harnesses the intrinsic medical knowledge of LLMs to bridge the semantic gap between im-
 195 ages and text, enabling more precise disease classification.

196 2.3 THE PROPOSED LLAVA-RADZ

197 We aim to learn generalizable medical image representations from radiology reports to enhance
 198 various downstream medical image recognition tasks, particularly when labeled data is scarce. The
 199 overall framework is illustrated in Fig. 3. Given a pair of medical images and reports, the image
 200 and text are first passed through separate visual and text encoders to obtain their respective encoded
 201 features. These encoded features and specially designed tokens are then fed into a language model
 202 to obtain the final feature representation. The features are mapped into a common representational
 203 space via an MLP projection layer and optimized with the InfoNCE loss. Furthermore, we propose
 204 a Domain Knowledge Anchor Module (DKAM), which leverages domain knowledge inherent in the
 205 model to guide the alignment of text and image features at the category level.

206 2.3.1 END-TO-END TRAINING STRATEGY

207 Currently, most MLLMs employ generation-based training objectives for instruction fine-tuning.
 208 Although this approach effectively captures the features of medical images and textual reports, its
 209 performance in zero-shot tasks remains suboptimal, as it fails to fully leverage these features. To
 210 address this issue, we propose a novel training strategy, Decoding-Side Feature Alignment Training
 211 (DFAT), as illustrated in Fig. 3.

212 We consider a training dataset consisting of N pairs of medical image-text samples, denoted as
 213 $S_{\text{train}} = \{(X_1, Y_1), \dots, (X_N, Y_N)\}$. The medical image $X_i \in \mathbb{R}^{H \times W \times 3}$, with H and W repre-

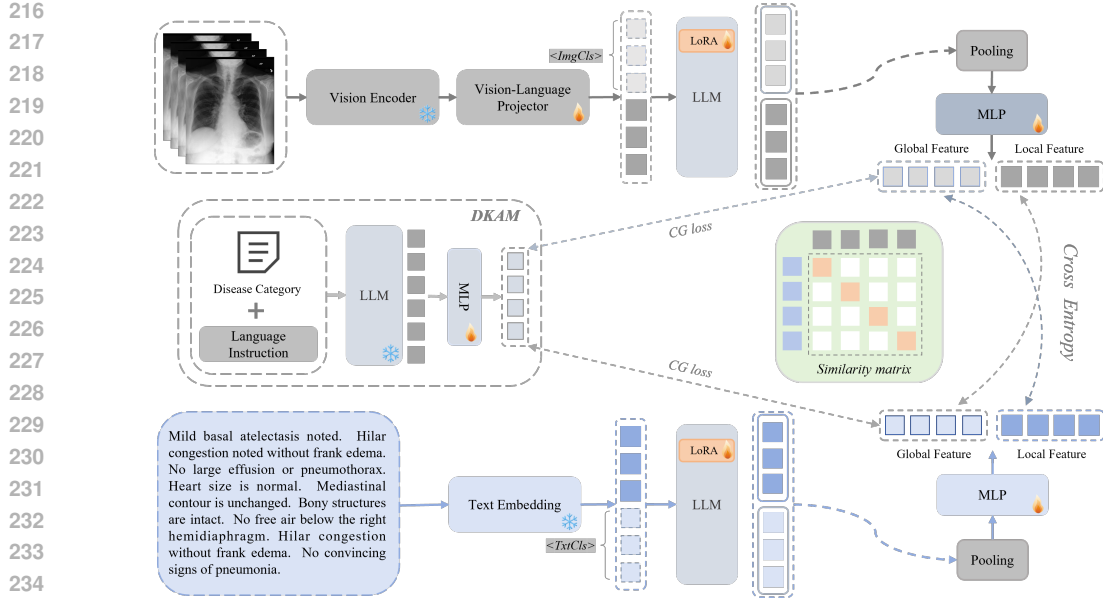


Figure 3: The LLaVA-RadZ framework consists of three components. (A) Construct a category semantic vector repository using the domain knowledge anchoring module (DKAM). (B) Encode medical images and text, appending $\langle \text{Img} \text{Cls}_i \rangle$ and $\langle \text{Txt} \text{Cls}_i \rangle$ tokens before feeding them into the LLM. (C) Extract global and local features, optimizing with cross-entropy loss, while leveraging the semantic repository for category-level alignment.

senting the height and width of the image, respectively. Y_i refers to the corresponding medical text report associated with the image.

Specifically, we design special tokens for both image and text modalities, where $\langle \text{Img} \text{Cls}_i \rangle$ ($i = 0, \dots, 4$) denotes image feature tokens and $\langle \text{Txt} \text{Cls}_i \rangle$ ($i = 0, \dots, 8$) denotes text feature tokens. These special tokens are attached to the image prompt X_{prompt} and the text prompt Y_{prompt} , respectively. The image prompt X_{prompt} has a format similar to “What disease is indicated by the chest X-ray?”, while the text prompt Y_{prompt} follows a format such as “What disease is described in this text?”. By appending special tokens, we obtain the modified prompts $\tilde{X}_{\text{prompt}}$ and $\tilde{Y}_{\text{prompt}}$, which is represented as:

$$\tilde{X}_{\text{prompt}} = X_{\text{prompt}} + \langle \text{Img} \text{Cls}_i \rangle_{(i=0, \dots, 4)}, \quad (1)$$

$$\tilde{Y}_{\text{prompt}} = Y_{\text{prompt}} + \langle \text{Txt} \text{Cls}_i \rangle_{(i=0, \dots, 8)}. \quad (2)$$

When an image and its corresponding prompt $\tilde{X}_{\text{prompt}}$ are input into the MLLM \mathcal{F} to generate a response \hat{R}_{img} . Similarly, when a text sample and its corresponding feature extraction prompt $\tilde{Y}_{\text{prompt}}$ are provided as input, the model produces a response \hat{R}_{txt} . This process can be formally expressed as:

$$\hat{R}_{\text{img}}^i = \mathcal{F}(X_i, \tilde{X}_{\text{prompt}}), \quad \hat{R}_{\text{txt}}^i = \mathcal{F}(Y_i, \tilde{Y}_{\text{prompt}}). \quad (3)$$

Due to the autoregressive nature of the decoder architecture, when the LLM processes visual and textual information to generate responses, its internal representations are stored in the designated special tokens. Specifically, we extract the penultimate layer embedding \tilde{h}_{img} corresponding to the special token $\langle \text{Img} \text{Cls}_i \rangle$, which stores the global image features $H_{\text{img}}^{\text{global}} \in \mathbb{R}^{B \times I \times K}$. Here, B denotes the number of image-text pairs in each batch, I represents the number of special image tokens, and K is the dimension of the shared embedding space. After applying a pooling operation followed by an MLP projection layer γ_{img} , we obtain the global image feature representation $X_g \in \mathbb{R}^{B \times K}$. The local image feature $X_l \in \mathbb{R}^{B \times K}$ is obtained by pooling the hidden states of all tokens except those corresponding to special tokens, followed by an MLP projection layer γ_{img} :

$$X_g = \gamma_{\text{img}}(\text{AvgPool}(H_{\text{img}}^{\text{global}})), \quad X_l = \gamma_{\text{img}}(\text{AvgPool}(H_{\text{img}}^{\text{local}})). \quad (4)$$

270 Similarly, we extract the global text representation $Y_g \in \mathbb{R}^{B \times K}$ and the local text representation
 271 $Y_l \in \mathbb{R}^{B \times K}$ using the same methodology:
 272

$$273 \quad Y_g = \gamma_{\text{txt}}(\text{AvgPool}(H_{\text{txt}}^{\text{global}})), \quad Y_l = \gamma_{\text{txt}}(\text{AvgPool}(H_{\text{txt}}^{\text{local}})). \quad (5)$$

275 To further enhance fine-grained alignment across different modalities, we introduce a cross-modal
 276 contrastive loss, L_{CA} . Specifically, for the i -th image-text pair (X_i, Y_i) in a batch, we alternately
 277 align the global and local features of images and texts. This procedure yields two symmetric,
 278 temperature-normalized InfoNCE objectives: one aligns global image features with local text fea-
 279 tures, and the other aligns local image features with global text features. These objectives maximize
 280 the mutual information between image-text pairs in the latent space.

281 For the alignment between global image features and local text features, we calculate two similarity
 282 matrices, $S_i^{X_g \rightarrow Y_l}$ and $S_i^{Y_l \rightarrow X_g}$, with the following computation:
 283

$$284 \quad S_i^{X_g \rightarrow Y_l} = \frac{X_{g,i} \cdot Y_{l,i}^T}{\tau}, \quad S_i^{Y_l \rightarrow X_g} = \frac{Y_{l,i} \cdot X_{g,i}^T}{\tau}. \quad (6)$$

286 where τ is the temperature hyperparameter. Subsequently, we compute the contrastive loss between
 287 the global image and the local text, with the following formula:
 288

$$289 \quad L_{CA}^{X_g \rightarrow Y_l, i} = -\log \frac{\exp(S_i^{X_g \rightarrow Y_l})}{\sum_{k=1}^B \exp(S_k^{X_g \rightarrow Y_l})}, \quad L_{CA}^{Y_l \rightarrow X_g, i} = -\log \frac{\exp(S_i^{Y_l \rightarrow X_g})}{\sum_{k=1}^B \exp(S_k^{Y_l \rightarrow X_g})}. \quad (7)$$

$$291 \quad L_{CA}^{X_g \rightarrow Y_l} = \frac{1}{2} \sum_{i=1}^B (L_{CA}^{X_g \rightarrow Y_l, i} + L_{CA}^{Y_l \rightarrow X_g, i}). \quad (8)$$

294 Similarly, for the alignment between local image features and global text features, we compute the
 295 contrastive loss between the local image and global text.
 296

$$297 \quad L_{CA}^{X_l \rightarrow Y_g} = -\frac{1}{2} \sum_{i=1}^B \left(\log \frac{\exp(S_i^{X_l \rightarrow Y_g})}{\sum_{k=1}^B \exp(S_k^{X_l \rightarrow Y_g})} + \log \frac{\exp(S_i^{Y_g \rightarrow X_l})}{\sum_{k=1}^B \exp(S_k^{Y_g \rightarrow X_l})} \right). \quad (9)$$

300 Finally, we obtain our cross-modal contrastive loss L_{CA} .
 301

$$301 \quad L_{CA} = \frac{1}{2} (L_{CA}^{X_g \rightarrow Y_l} + L_{CA}^{X_l \rightarrow Y_g}). \quad (10)$$

303 2.3.2 DOMAIN KNOWLEDGE ANCHOR MODULE

305 In aligning medical images with text reports, we observed that the critical entity of the medical
 306 disease categories was merely encoded as features by the model, without considering the underlying
 307 semantics. To address this limitation and further enhance fine-grained alignment capabilities, we
 308 introduce the Domain Knowledge Anchoring Module (DKAM). Initially, we leverage the inherent
 309 medical domain expertise of an LLM to generate descriptive explanations for each disease category.
 310 These generated disease descriptions serve as an intermediary bridge to guide the alignment between
 311 medical images and text reports. Specifically, we input the disease list D_{list} from the training dataset
 312 along with a designed prompt template K_{prompt} into the LLM \mathcal{F} . This process is formally expressed
 313 as:
 314

$$\hat{R}_{\text{dis}} = \mathcal{F}(D_{\text{list}}, K_{\text{prompt}}). \quad (11)$$

315 By fully harnessing the LLM's exceptional semantic understanding, we prompt the model to explore
 316 the underlying semantics of the disease categories and discern their distinctions, ultimately produc-
 317 ing a refined disease description. The features extracted from the LLM's response are then mapped
 318 via a multi-layer perceptron (MLP) to yield the disease description vector \hat{D} , which is represented
 319 as:
 320

$$\hat{D} = \gamma_{\text{dis}}(\hat{R}_{\text{dis}}). \quad (12)$$

322 Subsequently, we introduce the Category of Knowledge-guided Contrastive Loss L_{CG} . Specifically,
 323 we calculate the cross-entropy loss between the disease description vector \hat{D} and the global features
 324 of both the images X_g and the text Y_g . This design encourages the model to better capture the

324
 325 Table 1: Comparison of zero-shot disease classification performance of public MLLMs and LLaVA-
 326 based exploratory methods across five medical benchmarks. “ft” denotes supervised fine-tuning with
 327 LoRA, “CoT” refers to zero-shot chain-of-thought prompting templates, and “Inference” represents
 328 CLIP inference strategies. The best results are highlighted in bold and the second-best results are
 329 underlined.

329	Method	Dataset	CheXpert			ChestXray-14			COVIDx CXR-2			RSNA Pneumonia			SIIM-ACR		
			AUC ↑	F1 ↑	ACC ↑	AUC ↑	F1 ↑	ACC ↑	AUC ↑	F1 ↑	ACC ↑	AUC ↑	F1 ↑	ACC ↑	AUC ↑	F1 ↑	ACC ↑
330	MLLM	LLaVA-1.5 (7B) (Liu et al., 2023)	-	7.50	8.28	-	3.33	6.92	-	53.14	50.28	-	40.53	55.34	-	23.66	50.36
		LLaVA-Med (7B) (Li et al., 2024a)	-	6.87	8.94	-	8.02	6.78	-	34.90	50.03	-	18.58	50.00	-	21.91	49.90
		Qwen2.5-Max (Yang et al., 2024)	-	32.23	67.97	-	19.04	76.19	-	75.91	76.81	-	43.58	43.59	-	64.70	72.57
		Gemini2-Pro (Team et al., 2023)	-	35.01	76.08	-	14.16	77.78	-	62.84	62.90	-	44.23	51.43	-	61.43	72.03
		GPT4-0 (Achiam et al., 2023)	-	45.85	81.14	-	19.85	81.55	-	50.93	77.08	-	54.20	65.33	-	64.57	72.11
331	Explorative Methods	LLaVA-1.5-7B _{ft}	-	10.61	19.62	-	7.85	19.06	-	27.74	25.18	-	43.60	34.80	-	52.37	50.95
		LLaVA-Med-7B _{ft}	-	14.25	31.46	-	9.00	21.43	-	27.42	24.09	-	46.72	38.88	-	53.11	57.68
		LLaVA-Med-7B _{ft} + CoT (Zhang et al., 2024)	-	8.90	26.23	-	8.33	20.46	-	27.12	26.55	-	49.59	43.80	-	54.06	51.07
		LLaVA-Med-7B _{ft} + Inference (Zhang et al., 2024)	71.00	44.85	75.45	64.30	<u>21.73</u>	70.86	71.07	69.84	60.39	<u>77.51</u>	<u>69.85</u>	<u>72.90</u>	71.25	<u>68.26</u>	71.27
332	Ours	LLaVA-RadZo	<u>73.36</u>	48.59	<u>82.15</u>	<u>72.61</u>	27.91	<u>84.64</u>	<u>84.35</u>	<u>77.53</u>	74.58	86.98	76.18	<u>83.26</u>	89.92	79.57	84.38

333 Table 2: Comparison of performance with other SOTA methods on four medical datasets for the
 334 zero-shot classification task, with AUC, F1, and ACC scores reported. The best results are high-
 335 lighted in bold and the second-best results are underlined.

336	Method	ChestXray-14			COVIDx CXR-2			RSNA Pneumonia			SIIM-ACR		
		AUC ↑	F1 ↑	ACC ↑	AUC ↑	F1 ↑	ACC ↑	AUC ↑	F1 ↑	ACC ↑	AUC ↑	F1 ↑	ACC ↑
337	ConVIRT (Zhang et al., 2022)	53.15	12.38	57.88	62.78	71.23	63.84	79.21	55.67	75.08	64.25	42.87	53.42
338	GLoRIA (Huang et al., 2021)	55.92	14.20	59.47	64.52	70.78	60.21	70.37	48.19	70.54	54.71	40.39	47.15
339	BioViL (Boecking et al., 2022)	57.82	15.64	61.33	61.40	70.92	58.20	84.12	54.59	74.43	70.28	46.45	68.22
340	CheXzero (Tiu et al., 2022)	66.99	21.99	65.38	73.13	76.13	71.45	85.13	61.49	78.34	84.60	65.97	77.34
341	MedKLIP (Wu et al., 2023)	72.33	24.18	79.40	76.28	76.54	71.96	86.57	63.28	79.97	89.79	72.73	83.99
342	MAVL (Phan et al., 2024)	73.50	<u>26.25</u>	<u>82.77</u>	<u>83.86</u>	81.73	78.07	<u>86.91</u>	<u>63.41</u>	<u>82.42</u>	92.04	<u>77.95</u>	87.14
343	Ours	<u>72.61</u>	27.91	84.64	<u>84.36</u>	<u>77.53</u>	<u>74.58</u>	86.98	76.18	<u>83.28</u>	<u>89.92</u>	79.57	<u>84.38</u>

344 semantic relationships among images, text, and disease categories during training, achieving a more
 345 robust category-level alignment.

$$S_i^{\text{img-disease}} = \frac{X_{g,i} \cdot D^T}{\tau}, \quad S_i^{\text{txt-disease}} = \frac{Y_{g,i} \cdot D^T}{\tau}. \quad (13)$$

$$L_{\text{CG},i}^{\text{txt}} = -\log \frac{\exp(S_i^{\text{txt-disease}})}{\sum_{k=1}^N \exp(S_k^{\text{txt-disease}})}, \quad L_{\text{CG},i}^{\text{img}} = -\log \frac{\exp(S_i^{\text{img-disease}})}{\sum_{k=1}^N \exp(S_k^{\text{img-disease}})}. \quad (14)$$

351 Here, N represents the number of disease categories, B denotes the number of medical image-text
 352 pairs in each batch, and τ is the temperature hyperparameter. The final category of knowledge-
 353 guided loss is as follows:

$$L_{\text{CG}} = \frac{1}{2} \sum_{i=1}^B (L_{\text{CG},i}^{\text{txt}} + L_{\text{CG},i}^{\text{img}}). \quad (15)$$

354 By combining the category knowledge-guided loss and the cross-modal contrastive loss, the final
 355 objective function is defined as follows:

$$L_{\text{total}} = \lambda L_{\text{CA}} + (1 - \lambda) L_{\text{CG}}, \quad (16)$$

356 where λ is a balancing factor used to adjust the weights of the two losses, and it is set to 0.5 by
 357 default.

358 3 EXPERIMENTS

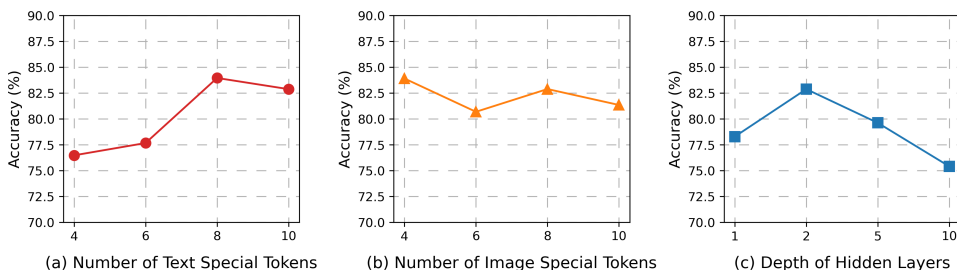
359 In this section, we first provide an overview of the dataset employed in our experiments, including
 360 those used for pre-training and the various downstream tasks. Subsequently, we outline the imple-
 361 mentation details and describe the baselines considered for comparison.

362 3.1 DATASET

363 In our experiments, we pre-trained the model using the MIMIC-CXR dataset (Johnson et al., 2019).
 364 For downstream tasks, we primarily evaluated the model’s performance in medical disease clas-
 365 sification using multiple benchmark datasets, including ChestX-ray14 (Wang et al., 2017), RSNA
 366 Pneumonia (Shih et al., 2019), SIIM-ACR Pneumothorax (sii, 2019), CheXpert (Irvin et al., 2019),
 367 and COVIDx CXR-2 (Pavlova et al., 2022). Detailed information on these datasets can be found in
 368 the supplementary material.

378
 379 Table 3: Comparison of performance with other SOTA methods at different data portions for fine-
 380 tuning classification task. AUC scores are reported. The best results are highlighted in bold and the
 381 second-best results are underlined.
 382

Method	RSNA Pneumonia			Pneumothorax			COVIDx CXR-2		
	1%	10%	100%	1%	10%	100%	1%	10%	100%
Scratch	68.94	83.31	87.12	53.11	76.18	87.48	85.11	93.65	98.86
ConVIRT (Zhang et al., 2022)	78.86	85.42	87.64	72.39	80.41	91.67	90.30	97.74	99.70
GLoRIA (Huang et al., 2021)	79.13	85.59	87.83	75.85	86.20	91.89	92.74	97.18	99.54
BioViL (Boecking et al., 2022)	80.27	86.04	88.29	70.29	79.45	88.05	92.39	98.39	99.68
MedKLIP (Wu et al., 2023)	82.11	87.14	88.58	85.24	89.91	93.02	95.58	98.77	99.77
MAVL (Phan et al., 2024)	86.09	87.90	88.94	91.53	93.00	94.48	97.18	99.15	99.90
Ours	88.23	88.57	89.49	88.42	89.96	94.50	98.32	99.80	99.96



390
 391 Figure 4: Effect of Special Token Numbers and Hidden Layer Depth on ChestXray-14 Classification.
 392
 393

400 3.2 EVALUATION METRICS 401

402 For the zero-shot classification task, we employ standard classification evaluation metrics, including
 403 Accuracy, AUC score, and F1 score. The macro-average metrics are reported for all diseases present
 404 in the target dataset.
 405

406 3.3 ZERO-SHOT EVALUATION 407

408 As shown in Tab. 2, we compare the performance of established methods in the field on the zero-shot
 409 classification task for radiological diseases, evaluated on four officially released test datasets. Our
 410 findings demonstrate that, compared to conventional CLIP-style models such as ConVIRT (Zhang
 411 et al., 2022), GLoRIA (Huang et al., 2021), BioViL (Boecking et al., 2022), and CheXzero (Tiu
 412 et al., 2022), our approach exhibits significant advantages. Even when compared to state-of-the-art
 413 models incorporating external models or domain-specific expert knowledge, our method remains
 414 highly competitive. Specifically, on the multi-class dataset ChestXray-14, our model surpasses the
 415 supervised learning method MAVL (Phan et al., 2024) by 1.87% in accuracy. Moreover, on the
 416 RSNA Pneumonia dataset, we achieve a 12.77% improvement in F1 score. These results indicate
 417 that multimodal large language models (MLLMs) possess strong feature extraction capabilities, fur-
 418 ther underscoring their immense potential in medical disease classification tasks.
 419

420 3.4 FINE-TUNING EVALUATION 421

422 Consistent with previous studies (Phan et al., 2024; Wu et al., 2023), we fine-tune the model on
 423 downstream datasets using 1%, 10%, and 100% of the available data and further evaluate its perfor-
 424 mance. Tab. 3 presents the fine-tuning results across three datasets, demonstrating that our model
 425 consistently maintains a competitive advantage. Notably, when fine-tuned with only 1% data, our
 426 proposed LLaVA-RadZ outperforms the MAVL (Phan et al., 2024) model by 2.14% on the RSNA
 427 Pneumonia and by 1.14% on COVIDx. Even when fine-tuned with 100% data, our model continues
 428 to deliver performance improvements. This enhancement is likely attributed to our decoder-side
 429 alignment training strategy, which effectively captures global modality information and leverages
 430 the interaction between global and local features to achieve fine-grained cross-modal alignment,
 431 further strengthening the model’s disease recognition capability.
 432

432
 433 Table 4: Ablation study of DKAM on ChestXray-14.
 434 D_1 represents a semantic vector library of 75 medical
 435 entities, and D_2 represents a semantic vector library of
 436 14 disease categories.
 437

#	DKAM	D_1	D_2	AUC \uparrow	F1 \uparrow	ACC \uparrow
a				69.31	27.30	82.32
b	✓	✓		68.67	25.73	81.84
c	✓		✓	72.61	27.91	84.64

439 3.5 ABLATION STUDY

440
 441 **Ablation Study of DKAM.** To validate the effectiveness of our proposed Domain Knowledge
 442 Anchor Module (DKAM), we conducted an ablation study on the ChestXray-14 dataset. With DKAM
 443 incorporated, we further investigated the impact of different category semantic vector repositories
 444 on the model’s fine-grained alignment capability. Consistent with the previous MedKLIP study, we
 445 selected 75 primary medical entities from the MIMIC-CXR dataset. However, unlike MedKLIP, we
 446 leveraged the model’s intrinsic domain knowledge to construct a category semantic vector reposi-
 447 tory, denoted as D_1 . Additionally, we built a disease-specific semantic vector repository for the 14
 448 medical disease categories present in the MIMIC-CXR training dataset, denoted as D_2 .

449 As shown in Tab. 4 (a vs. c), the introduction of DKAM significantly enhances model performance.
 450 Using disease category semantics as an intermediary facilitates more precise alignment between
 451 medical images and textual descriptions at the category level. Further comparisons in Tab. 4 (b vs.
 452 c) demonstrate that, compared to a larger repository of medical entities, a semantic vector repository
 453 focusing on primary disease categories provides stronger guidance for image-text alignment. More-
 454 over, additional medical entities in D_1 , such as tip, tube, PICC, and device, may introduce noise and
 455 negatively impact alignment at the disease category level. This adverse effect is corroborated by the
 456 comparative results in Tab. 4 (a vs. b).

457 **Ablation Study of Special Tokens.** As shown in Tab. 1, we have demonstrated the effectiveness of
 458 the Decoding-Side Feature Alignment Training (DFAT) strategy. To further investigate the design
 459 of the critical special tokens integral to this approach, we conducted an in-depth analysis on the
 460 ChestXray-14 dataset. As illustrated in Fig. 4, we observed that the number of text and image
 461 tokens significantly influences model performance, with both an excessive and an insufficient count
 462 potentially resulting in a loss of modal information. Moreover, our study indicates that the optimal
 463 global features are not stored in the final hidden layer but rather in the penultimate layer, which
 464 may be attributed to the loss of fine-grained information due to deeper feature aggregation, thereby
 465 affecting overall performance.

466 **Ablation Study of Features.** During the process of cross-modal alignment, we conducted a detailed
 467 analysis of the impact of global and local features on model performance, and further investigated the
 468 effectiveness of using prompts, as shown in Tab. 5. The experimental results indicate that utilizing
 469 only local features yields the poorest performance, while relying solely on global features provides
 470 a certain advantage over local features. This may be attributed to the fact that the specially designed
 471 tokens for each modality can more precisely capture the global information of the corresponding
 472 modality. Moreover, the combination of global and local features achieves the best performance.
 473 Additionally, the incorporation of prompts further enhances the model’s ability to capture feature
 474 information.

475 4 CONCLUSION

476 This paper proposes a simple yet effective framework, LLaVA-RadZ, for zero-shot medical
 477 disease recognition. First, we introduce an end-to-end decoding-side feature alignment training strat-
 478 egy to leverage the characteristics of the MLLM architecture and effectively store modality-related
 479 information. Additionally, we employ cross-modal contrastive learning to optimize feature align-
 480 ment across modalities, enhancing the model’s cross-modal understanding capabilities. Further-
 481 more, we propose a domain knowledge anchoring Module to facilitate category-level alignment
 482 between medical images and textual descriptions. Experimental results demonstrate that LLaVA-
 483 RadZ achieves outstanding performance across multiple benchmarks, highlighting the significant
 484 potential of MLLMs in tackling zero-shot radiological disease recognition tasks.

485 Table 5: Ablation study of feature representations on
 ChestXray-14.

#	Global	Local	Prompt	AUC \uparrow	F1 \uparrow	ACC \uparrow
a		✓		67.14	25.11	77.82
b		✓	✓	68.29	26.42	78.63
c	✓		✓	70.13	26.22	82.50
d	✓	✓	✓	72.61	27.91	84.64

486
487
ETHICS STATEMENT488
489
490
491
492
493
494
495
This study follows the ICLR Code of Ethics. All experiments and data usage comply with relevant
laws, regulations, and ethical requirements. The data used are from publicly available datasets or
obtained with proper authorization, and have been appropriately preprocessed to ensure privacy
and security. This work aims to advance scientific research and is not intended for any harmful or
inappropriate applications. The authors declare no conflict of interest.496
497
498
499
REPRODUCIBILITY STATEMENT500
501
502
503
504
505
506
507
We provide detailed descriptions of our methods, datasets, and experimental settings in the main
text and appendix. All source code and data processing scripts will be made publicly available
upon publication to facilitate reproducibility. Additional implementation details are available in the
supplementary materials.508
509
510
REFERENCES511
512
513
514
515
516
517
518
519
520
521
522
523
524
525
526
527
528
529
530
531
532
533
534
535
536
537
538
539
Society for imaging informatics in medicine: Siim-acr pneumothorax segmentation. <https://www.kaggle.com/c/siim-acr-pneumothorax-segmentation>, 2019.
Josh Achiam, Steven Adler, Sandhini Agarwal, Lama Ahmad, Ilge Akkaya, Florencia Leoni Aleman, Diogo Almeida, Janko Altenschmidt, Sam Altman, Shyamal Anadkat, et al. Gpt-4 technical report. *arXiv preprint arXiv:2303.08774*, 2023.
Olivier Bodenreider. The unified medical language system (umls): integrating biomedical terminology. *Nucleic acids research*, 32(suppl_1):D267–D270, 2004.
Benedikt Boecking, Naoto Usuyama, Shruthi Bannur, Daniel C Castro, Anton Schwaighofer, Stephanie Hyland, Maria Wetscherek, Tristan Naumann, Aditya Nori, Javier Alvarez-Valle, et al. Making the most of text semantics to improve biomedical vision–language processing. In *European conference on computer vision*, pp. 1–21. Springer, 2022.
Heang-Ping Chan, Lubomir M Hadjiiski, and Ravi K Samala. Computer-aided diagnosis in the era of deep learning. *Medical physics*, 47(5):e218–e227, 2020.
Aakanksha Chowdhery, Sharan Narang, Jacob Devlin, Maarten Bosma, Gaurav Mishra, Adam Roberts, Paul Barham, Hyung Won Chung, Charles Sutton, Sebastian Gehrmann, et al. Palm: Scaling language modeling with pathways. *Journal of Machine Learning Research*, 24(240):1–113, 2023.
Shivang Desai, Ahmad Baghal, Thidathip Wongsurawat, Piroon Jenjaroenpun, Thomas Powell, Shaymaa Al-Shukri, Kim Gates, Phillip Farmer, Michael Rutherford, Geri Blake, et al. Chest imaging representing a covid-19 positive rural us population. *Scientific data*, 7(1):414, 2020.
Tianyu Han, Lisa C Adams, Jens-Michalis Papaioannou, Paul Grundmann, Tom Oberhauser, Alexander Löser, Daniel Truhn, and Keno K Bressem. Medalpac-a-an open-source collection of medical conversational ai models and training data. *arXiv preprint arXiv:2304.08247*, 2023.
Hulingxiao He, Geng Li, Zijun Geng, Jinglin Xu, and Yuxin Peng. Analyzing and boosting the power of fine-grained visual recognition for multi-modal large language models. *arXiv preprint arXiv:2501.15140*, 2025.
Shih-Cheng Huang, Liyue Shen, Matthew P Lungren, and Serena Yeung. Gloria: A multimodal global-local representation learning framework for label-efficient medical image recognition. In *Proceedings of the IEEE/CVF International Conference on Computer Vision*, pp. 3942–3951, 2021.
Wenxuan Huang, Zijie Zhai, Yunhang Shen, Shaoshen Cao, Fei Zhao, Xiangfeng Xu, Zheyu Ye, and Shao-hui Lin. Dynamic-llava: Efficient multimodal large language models via dynamic vision-language context sparsification. *arXiv preprint arXiv:2412.00876*, 2024.
Wenxuan Huang, Bohan Jia, Zijie Zhai, Shaosheng Cao, Zheyu Ye, Fei Zhao, Zhe Xu, Yao Hu, and Shaohui Lin. Vision-r1: Incentivizing reasoning capability in multimodal large language models. *arXiv preprint arXiv:2503.06749*, 2025.

540 Jeremy Irvin, Pranav Rajpurkar, Michael Ko, Yifan Yu, Silviana Ciurea-Ilcus, Chris Chute, Henrik Marklund,
 541 Behzad Haghgoo, Robyn Ball, Katie Shpanskaya, et al. Chexpert: A large chest radiograph dataset with
 542 uncertainty labels and expert comparison. In *Proceedings of the AAAI conference on artificial intelligence*,
 543 volume 33, pp. 590–597, 2019.

544 Mohammad Jamshidi, Ali Lalbakhsh, Jakub Talla, Zdeněk Peroutka, Farimah Hadjilooei, Pedram Lalbakhsh,
 545 Morteza Jamshidi, Luigi La Spada, Mirhamed Mirmozafari, Mojgan Dehghani, et al. Artificial intelligence
 546 and covid-19: deep learning approaches for diagnosis and treatment. *Ieee Access*, 8:109581–109595, 2020.

547 Alistair EW Johnson, Tom J Pollard, Seth J Berkowitz, Nathaniel R Greenbaum, Matthew P Lungren, Chih-
 548 ying Deng, Roger G Mark, and Steven Horng. Mimic-cxr, a de-identified publicly available database of
 549 chest radiographs with free-text reports. *Scientific data*, 6(1):317, 2019.

550 Haoran Lai, Qingsong Yao, Zihang Jiang, Rongsheng Wang, Zhiyang He, Xiaodong Tao, and S Kevin Zhou.
 551 Carzero: Cross-attention alignment for radiology zero-shot classification. In *Proceedings of the IEEE/CVF*
 552 *Conference on Computer Vision and Pattern Recognition*, pp. 11137–11146, 2024.

553 Junghwan Lee, Cong Liu, Junyoung Kim, Zhehuan Chen, Yingcheng Sun, James R Rogers, Wendy K Chung,
 554 and Chunhua Weng. Deep learning for rare disease: A scoping review. *Journal of biomedical informatics*,
 555 135:104227, 2022.

556 Chunyuan Li, Cliff Wong, Sheng Zhang, Naoto Usuyama, Haotian Liu, Jianwei Yang, Tristan Naumann, Hoi-
 557 fung Poon, and Jianfeng Gao. Llava-med: Training a large language-and-vision assistant for biomedicine in
 558 one day. *Advances in Neural Information Processing Systems*, 36, 2024a.

559 Jiachun Li, Pengfei Cao, Chenhao Wang, Zhuoran Jin, Yubo Chen, Daojian Zeng, Kang Liu, and Jun Zhao.
 560 Focus on your question! interpreting and mitigating toxic cot problems in commonsense reasoning. *arXiv*
 561 *preprint arXiv:2402.18344*, 2024b.

562 Junnan Li, Dongxu Li, Silvio Savarese, and Steven Hoi. Blip-2: Bootstrapping language-image pre-training
 563 with frozen image encoders and large language models. In *International conference on machine learning*,
 564 pp. 19730–19742. PMLR, 2023a.

565 Yunxiang Li, Zihan Li, Kai Zhang, Ruilong Dan, Steve Jiang, and You Zhang. Chatdoctor: A medical chat
 566 model fine-tuned on a large language model meta-ai (llama) using medical domain knowledge. *Cureus*, 15
 567 (6), 2023b.

568 Haotian Liu, Chunyuan Li, Qingyang Wu, and Yong Jae Lee. Visual instruction tuning. *Advances in neural*
 569 *information processing systems*, 36:34892–34916, 2023.

570 Yanming Liu, Xinyue Peng, Tianyu Du, Jianwei Yin, Weihao Liu, and Xuhong Zhang. Era-cot: improving
 571 chain-of-thought through entity relationship analysis. *arXiv preprint arXiv:2403.06932*, 2024.

572 Brandon McKinzie, Zhe Gan, Jean-Philippe Fauconnier, Sam Dodge, Bowen Zhang, Philipp Dufter, Dhruti
 573 Shah, Xianzhi Du, Futang Peng, Anton Belyi, et al. Mml1: methods, analysis and insights from multimodal
 574 llm pre-training. In *European Conference on Computer Vision*, pp. 304–323. Springer, 2024.

575 Debjyoti Mondal, Suraj Modi, Subhadarshi Panda, Rituraj Singh, and Godawari Sudhakar Rao. Kam-cot:
 576 Knowledge augmented multimodal chain-of-thoughts reasoning. In *Proceedings of the AAAI conference on*
 577 *artificial intelligence*, volume 38, pp. 18798–18806, 2024.

578 Michael Moor, Qian Huang, Shirley Wu, Michihiro Yasunaga, Yash Dalmia, Jure Leskovec, Cyril Zakka,
 579 Eduardo Pontes Reis, and Pranav Rajpurkar. Med-flamingo: a multimodal medical few-shot learner. In
 580 *Machine Learning for Health (ML4H)*, pp. 353–367. PMLR, 2023.

581 Maya Pavlova, Naomi Terhljan, Audrey G Chung, Andy Zhao, Siddharth Surana, Hossein Aboutalebi, Hayden
 582 Gunraj, Ali Sabri, Amer Alaref, and Alexander Wong. Covid-net cxr-2: An enhanced deep convolutional
 583 neural network design for detection of covid-19 cases from chest x-ray images. *Frontiers in Medicine*, 9:
 584 861680, 2022.

585 Vu Minh Hieu Phan, Yutong Xie, Yuankai Qi, Lingqiao Liu, Liyang Liu, Bowen Zhang, Zhibin Liao, Qi Wu,
 586 Minh-Son To, and Johan W Verjans. Decomposing disease descriptions for enhanced pathology detection:
 587 A multi-aspect vision-language pre-training framework. In *Proceedings of the IEEE/CVF Conference on*
 588 *Computer Vision and Pattern Recognition*, pp. 11492–11501, 2024.

589 Alec Radford, Jong Wook Kim, Chris Hallacy, Aditya Ramesh, Gabriel Goh, Sandhini Agarwal, Girish Sas-
 590 try, Amanda Askell, Pamela Mishkin, Jack Clark, et al. Learning transferable visual models from natural
 591 language supervision. In *International conference on machine learning*, pp. 8748–8763. PmLR, 2021.

594 Hao Shao, Shengju Qian, Han Xiao, Guanglu Song, Zhuofan Zong, Letian Wang, Yu Liu, and Hongsheng
 595 Li. Visual cot: Advancing multi-modal language models with a comprehensive dataset and benchmark for
 596 chain-of-thought reasoning. *Advances in Neural Information Processing Systems*, 37:8612–8642, 2024.

597 George Shih, Carol C Wu, Safwan S Halabi, Marc D Kohli, Luciano M Prevedello, Tessa S Cook, Arjun
 598 Sharma, Judith K Amorosa, Veronica Arteaga, Maya Galperin-Aizenberg, et al. Augmenting the national
 599 institutes of health chest radiograph dataset with expert annotations of possible pneumonia. *Radiology: Artificial Intelligence*, 1(1):e180041, 2019.

600 601 Karan Singhal, Shekoofeh Azizi, Tao Tu, S Sara Mahdavi, Jason Wei, Hyung Won Chung, Nathan Scales, Ajay
 602 Tanwani, Heather Cole-Lewis, Stephen Pfohl, et al. Large language models encode clinical knowledge. *Nature*, 620(7972):172–180, 2023.

603 604 Gemini Team, Rohan Anil, Sebastian Borgeaud, Jean-Baptiste Alayrac, Jiahui Yu, Radu Soricu, Johan Schalkwyk, Andrew M Dai, Anja Hauth, Katie Millican, et al. Gemini: a family of highly capable multimodal models. *arXiv preprint arXiv:2312.11805*, 2023.

605 606 607 Ekin Tiu, Ellie Talius, Pujan Patel, Curtis P Langlotz, Andrew Y Ng, and Pranav Rajpurkar. Expert-level detection of pathologies from unannotated chest x-ray images via self-supervised learning. *Nature biomedical engineering*, 6(12):1399–1406, 2022.

608 609 610 Shengbang Tong, Zhuang Liu, Yuexiang Zhai, Yi Ma, Yann LeCun, and Saining Xie. Eyes wide shut? exploring the visual shortcomings of multimodal llms. In *Proceedings of the IEEE/CVF Conference on Computer Vision and Pattern Recognition*, pp. 9568–9578, 2024.

611 612 613 Khoa A Tran, Olga Kondrashova, Andrew Bradley, Elizabeth D Williams, John V Pearson, and Nicola Waddell. Deep learning in cancer diagnosis, prognosis and treatment selection. *Genome medicine*, 13:1–17, 2021.

614 615 616 Xiaosong Wang, Yifan Peng, Le Lu, Zhiyong Lu, Mohammadhadhi Bagheri, and Ronald M Summers. Chestx-ray8: Hospital-scale chest x-ray database and benchmarks on weakly-supervised classification and localization of common thorax diseases. In *Proceedings of the IEEE conference on computer vision and pattern recognition*, pp. 2097–2106, 2017.

617 618 619 Chaoyi Wu, Xiaoman Zhang, Ya Zhang, Yanfeng Wang, and Weidi Xie. Medklip: Medical knowledge enhanced language-image pre-training for x-ray diagnosis. In *Proceedings of the IEEE/CVF International Conference on Computer Vision*, pp. 21372–21383, 2023.

620 621 622 An Yang, Baosong Yang, Beichen Zhang, Binyuan Hui, Bo Zheng, Bowen Yu, Chengyuan Li, Dayiheng Liu, Fei Huang, Haoran Wei, et al. Qwen2. 5 technical report. *arXiv preprint arXiv:2412.15115*, 2024.

623 624 625 Ling You, Wenxuan Huang, Xinni Xie, Xiangyi Wei, Bangyan Li, Shaohui Lin, Yang Li, and Changbo Wang. Timesoccer: An end-to-end multimodal large language model for soccer commentary generation. *arXiv preprint arXiv:2504.17365*, 2025.

626 627 628 Sheng Zhang, Yanbo Xu, Naoto Usuyama, Jaspreet Bagga, Robert Tinn, Sam Preston, Rajesh Rao, Mu Wei, Naveen Valluri, Cliff Wong, et al. Large-scale domain-specific pretraining for biomedical vision-language processing. *arXiv preprint arXiv:2303.00915*, 2(3):6, 2023a.

629 630 631 Xiaoman Zhang, Chaoyi Wu, Ya Zhang, Weidi Xie, and Yanfeng Wang. Knowledge-enhanced visual-language pre-training on chest radiology images. *Nature Communications*, 14(1):4542, 2023b.

632 633 634 Yuhao Zhang, Hang Jiang, Yasuhide Miura, Christopher D Manning, and Curtis P Langlotz. Contrastive learning of medical visual representations from paired images and text. In *Machine Learning for Healthcare Conference*, pp. 2–25. PMLR, 2022.

635 636 637 Yuhui Zhang, Alyssa Unell, Xiaohan Wang, Dhruba Ghosh, Yuchang Su, Ludwig Schmidt, and Serena Yeung-Levy. Why are visually-grounded language models bad at image classification? *The Thirty-eighth Annual Conference on Neural Information Processing Systems*, 2024.

638 639 640 Deyao Zhu, Jun Chen, Xiaoqian Shen, Xiang Li, and Mohamed Elhoseiny. Minigpt-4: Enhancing vision-language understanding with advanced large language models. *arXiv preprint arXiv:2304.10592*, 2023.

641 642 643 644 645 646 647

648 A RELATED WORK
649650 **Multi-modal Large Language Models.** Inspired by the exceptional reasoning capabilities of
651 large language models (LLMs), researchers are actively exploring ways to extend these abilities
652 to the visual domain, driving advancements in multimodal LLMs. With the release of GPT-4 (Vi-
653 sion) (Achiam et al., 2023) and Gemini (Team et al., 2023), these models have demonstrated remark-
654 able multimodal understanding and generation capabilities, further fueling research in this field.
655656 To bridge the gap between vision encoders and LLMs, BLIP-2 (Li et al., 2023a) introduces a Q-
657 Former that transforms image features into a format compatible with LLMs, enabling seamless
658 integration with text embeddings. LLaVA (Liu et al., 2023) and MiniGPT-4 (Zhu et al., 2023)
659 further enhance generalization and task performance by leveraging large-scale multimodal pretrain-
660 ing, followed by instruction tuning for specific applications. In the medical domain, LLMs have
661 shown immense potential for advancing research and practical applications. Med-Flamingo (Moor
662 et al., 2023) extends Flamingo to the medical field by pretraining on multimodal knowledge sources
663 spanning multiple medical disciplines. LLaVA-Med (Li et al., 2024a) refines image-text pairs from
664 PMC-15M (Zhang et al., 2023a) and trains a biomedical-specialized MLLM using a limited dataset,
665 building upon the pre-trained parameters of LLaVA. Similarly, Med-PaLM (Singhal et al., 2023)
666 fine-tunes PaLM (Chowdhery et al., 2023) using domain-specific medical instructions, demon-
667 strating strong performance under human evaluation frameworks. Other notable models, such as Chat-
668 Doctor (Li et al., 2023b) and Med-Alpaca (Han et al., 2023), have been tailored for medical question-
669 answering and dialogue applications.670 Despite the significant progress of MLLMs, several challenges remain (McKinzie et al., 2024; Tong
671 et al., 2024; Zhang et al., 2024; He et al., 2025). Recent studies (Zhang et al., 2024; He et al., 2025)
672 highlight the suboptimal performance of MLLMs in image classification, particularly in fine-grained
673 category recognition. We find that this issue is especially pronounced in the medical domain, where
674 precise classification is crucial for medical applications. To address these shortcomings, we are
675 refining traditional MLLM training paradigms to enhance classification performance and improve
676 fine-grained category comprehension.677 **Prompt Engineering.** Prompting enhances the ability of pre-trained large language models (LLMs)
678 to understand tasks by incorporating language instructions into the input text (Mondal et al., 2024;
679 Shao et al., 2024; Liu et al., 2024; Li et al., 2024b). Recently, prompt-based techniques have also
680 been applied to vision-language models to improve performance. In medical vision-language
681 models (VLMs), GloRIA (Huang et al., 2021) generates a set of textual prompts to describe potential
682 subtypes, severity levels, and anatomical locations for each disease category. MedKLIP (Wu et al.,
683 2023) enhances model performance by retrieving descriptions of medical entities from the UMLS
684 knowledge base (Bodenreider, 2004). CARZero (Lai et al., 2024) introduces a prompt-alignment
685 strategy based on LLMs, integrating prompt templates into the training dataset to ensure alignment
686 during both training and inference. MAVL (Phan et al., 2024) uses visual descriptions of pathologi-
687 cal features to guide the model in effectively detecting diseases in medical images.688 Although these approaches have successfully improved model performance through prompt-based
689 strategies, they all rely on external models or expert knowledge, without fully leveraging the model’s
690 intrinsic understanding capabilities. Fortunately, recent research on LLaVA-Med (Li et al., 2024a)
691 has demonstrated remarkable domain-specific conversational abilities, proving that it possesses a
692 certain level of medical knowledge. Building upon LLaVA-Med (Li et al., 2024a), we further ex-
693 plore the feasibility of utilizing the model’s inherent comprehension to enhance zero-shot medical
694 classification performance.695 B DATASET DETAILS
696697 **MIMIC-CXR v2 (Johnson et al., 2019).** In our experiments, we pre-trained the model using the
698 MIMIC-CXR, a publicly available collection of chest radiographs paired with corresponding radi-
699 ology text reports. The MIMIC-CXR dataset comprises 377,110 images corresponding to 227,835
700 radiographic studies from 65,379 patients. Since all downstream tasks utilize frontal-view images,
701 we exclude all lateral-view images from the dataset. Moreover, we selectively retain only the find-
702 ings and impressions sections from these reports.

702 **ChestX-ray14 (Wang et al., 2017).** ChestX-ray14 consists of 112,120 frontal-view chest X-ray images from 30,805 unique patients, collected between 1992 and 2015. The official test set, comprising 22,433 images, has been meticulously annotated by board-certified radiologists. For evaluation purposes, we restrict our testing to the official test set.

703 **RSNA Pneumonia (Shih et al., 2019).** RSNA Pneumonia includes over 260,000 frontal-view chest X-rays with annotated pneumonia masks, collected by the Radiological Society of North America (RSNA). This dataset supports both pneumonia segmentation and classification tasks (Wu et al., 704 2023; Phan et al., 2024). We partition the dataset into training, validation, and test sets with a ratio 705 of 0.6/0.2/0.2, respectively.

706 **SIIM-ACR Pneumothorax (sii, 2019).** SIIM-ACR Pneumothorax contains 12,954 chest X-ray images, along with image-level pneumothorax annotations and pixel-level segmentation masks where 707 pneumothorax is present. Like the RSNA Pneumonia dataset, it can be used for both classification 708 and segmentation tasks. We divide the dataset into training, validation, and test sets with a ratio of 709 0.6/0.2/0.2.

710 **CheXpert (Irvin et al., 2019).** CheXpert contains 224,316 chest X-ray images from 65,240 patients, 711 collected by Stanford Hospital. The official test set includes images from 500 patients, annotated 712 through consensus by five board-certified radiologists. We evaluated all disease categories in this 713 test dataset.

714 **COVIDx CXR-2 (Pavlova et al., 2022) and COVID Rural (Desai et al., 2020).** The COVIDx CXR-2 and COVID Rural are designed for evaluating COVID-19 diagnosis. COVIDx CXR-2 (Pavlova et al., 2022) consists of 29,986 images from 16,648 COVID-19 patients, each labeled 715 with a classification tag. The dataset is split into training, validation, and test sets with a ratio of 0.7/0.2/0.1, used for evaluating classification performance. The COVID Rural dataset contains over 716 200 chest X-ray images with annotated segmentation masks, used for the COVID-19 segmentation 717 task. This dataset is partitioned into training, validation, and test sets with a ratio of 0.6/0.2/0.2.

718 C MEDICAL CATEGORY SEMANTIC VECTOR LIBRARY

719 We draw inspiration from the work of MedKLIP (Wu et al., 2023) and incorporate 75 frequently 720 occurring medical entities from clinical reports as input to our model. By designing prompts, we 721 stimulate the model’s intrinsic medical knowledge, enabling it to infer the semantic representations 722 of various entity categories. The resulting semantic descriptions of these 75 medical entities are 723 presented in table 7.

724 Furthermore, to achieve a more precise representation of major disease categories, we construct 725 a dedicated disease semantic vector library, which facilitates a more nuanced understanding of 726 disease-related semantics. The generated disease descriptions are detailed in table 6.

727 D IMPLEMENTATION DETAILS

728 Unless otherwise specified, we use LLaVA-Med (Li et al., 2024a) as the foundational MLLM \mathcal{F} . 729 We employ the LoRA strategy for parameter-efficient fine-tuning, with training managed via the 730 DeepSpeed engine.

731 For optimization, we utilize the AdamW optimizer with a learning rate of 2e-5 and no weight decay. 732 A cosine learning rate decay schedule is applied, with 3% of the total training steps allocated for 733 warm-up. The number of special tokens for images $\langle ImgClz \rangle$ is set to 4, while the number of 734 special tokens for text $\langle TxtClz \rangle$ is set to 8. The temperature hyperparameter τ is configured as 735 0.05, and the loss weight coefficient λ is set to 0.5. Furthermore, the batch size per GPU is set to 64.

736 E USE OF LLMs

737 This paper employed large language models (i.e., ChatGPT, Claude) solely for language editing and 738 polishing purposes, including but not limited to grammar checking, expression optimization, and text 739 refinement. All core research content, including experimental design, data analysis, and conclusion

756 derivation, was carried out independently by the authors. The authors take full responsibility for the
757 entire content of this paper and have thoroughly verified and validated all AI-assisted modifications.
758
759
760
761
762
763
764
765
766
767
768
769
770
771
772
773
774
775
776
777
778
779
780
781
782
783
784
785
786
787
788
789
790
791
792
793
794
795
796
797
798
799
800
801
802
803
804
805
806
807
808
809

Table 6: Semantic Descriptions of 14 Medical Disease Categories

Disease	Description
Fibrosis	Fibrosis refers to excessive deposition of collagen and extracellular matrix during abnormal tissue repair after inflammation or injury, leading to the replacement of normal lung tissue with reticular or band-like high-density shadows, commonly seen in the lower and peripheral lungs. Imaging may show honeycombing and traction bronchiectasis. Clinically, patients often present with progressive dyspnea, dry cough, and reduced exercise tolerance.
Edema	Pulmonary edema refers to the abnormal accumulation of fluid in the pulmonary interstitium and alveoli, usually caused by cardiogenic or non-cardiogenic factors. Imaging shows patchy or 'bat-wing' distributed heterogeneous high-density shadows in the middle or entire lung, often accompanied by Kerley lines and cardiac enlargement. Clinically, patients typically experience acute dyspnea, cough, cyanosis, and bilateral lung crackles.
Pneumothorax	Pneumothorax refers to the presence of air in the pleural cavity, leading to partial or complete lung collapse. Imaging typically shows a low-density black air space along the pleura, with a clear demarcation from the normal lung tissue, along with lung collapse. In tension pneumothorax, mediastinal shift may occur. Clinically, patients often present with sudden unilateral chest pain, dyspnea, and decreased breath sounds, sometimes accompanied by subcutaneous emphysema.
Cardiomegaly	Cardiomegaly refers to the enlargement of the heart due to hypertension, cardiomyopathy, or valvular disease, causing chamber dilation or wall thickening. Imaging shows significant cardiac enlargement with an expanded and smooth contour, often marked by an increased cardiothoracic ratio, potentially accompanied by pulmonary congestion and bronchial congestion. Clinically, patients may experience reduced exercise tolerance, dyspnea, lower limb edema, and arrhythmias.
Atelectasis	Atelectasis refers to the collapse of part or all of the lung tissue due to airway obstruction, external thoracic pressure, or intrapulmonary pathology. Imaging shows increased local lung density, volume reduction, bronchial displacement, and visceral pleural traction, commonly affecting the lower lobes. Clinically, patients may exhibit rapid shallow breathing, localized decreased or absent breath sounds, and a history of recent surgery or inadequate airway clearance.
Nodule	A lung nodule is a localized lesion with a diameter of less than 3 cm. Imaging typically shows a round or oval localized density, with either well-defined or spiculated edges. Some nodules may contain calcifications or low-density necrotic areas. Clinically, most patients are asymptomatic, but growing or malignant nodules may present with cough and hemoptysis.
Emphysema	Emphysema is a chronic obstructive pulmonary disease caused by the permanent destruction of alveolar walls and airspace enlargement. Imaging shows scattered or diffuse low-density areas in both lungs, reduced lung markings, often with bullae or cystic lesions, a flattened diaphragm, and hyperinflated lungs. Clinically, patients typically have a history of chronic cough, sputum production, and progressive dyspnea, often associated with smoking or long-term occupational exposure.
No Finding	No finding refers to the absence of radiographic abnormalities detected in the chest X-ray.

Table 6: Semantic Descriptions of 14 Medical Disease Categories

Disease	Description
Mass	A mass refers to an abnormal localized tissue overgrowth. Imaging shows a focal high-density lesion, which may have regular or irregular shapes with spiculated margins, often accompanied by internal necrosis, calcification, or hemorrhage. Surrounding features may include bronchial distortion or lymphadenopathy. Clinically, patients may present with cough, weight loss, or hemoptysis, requiring further pathological examination.
Pleural Thickening	Pleural thickening refers to fibrotic or calcified pleural changes due to chronic inflammation, infection, or asbestos exposure. Imaging shows localized or diffuse thickening along the pleural surface, appearing as streaky or patchy high-density shadows, sometimes with nodular changes. Clinically, patients may be asymptomatic, but a history of pleuritis or exposure to harmful substances is often present.
Effusion	Pleural effusion refers to the abnormal accumulation of fluid in the pleural cavity, which may be caused by infection, heart failure, malignancy, or other inflammatory diseases. Typically seen in the lower lung fields and posterior chest cavity, imaging shows a homogeneous or layered fluid density with a clear meniscus sign, with CT revealing low-density regions. Severe effusion may cause lung compression or bronchial displacement. Clinically, patients may present with dyspnea, chest pain, and cough, with physical signs of reduced breath sounds, dull percussion, and abnormal auscultation.
Infiltration	Infiltration refers to localized or diffuse high-density changes in lung tissue due to inflammation, infection, or malignancy. Imaging typically shows patchy or ill-defined high-density areas, sometimes with a ground-glass appearance or consolidation, occasionally accompanied by air bronchograms or bronchial wall thickening. Clinically, patients may present with cough, fever, dyspnea, and fatigue, often with elevated inflammatory markers.
Pneumonia	Pneumonia refers to lung parenchyma inflammation caused by bacteria, viruses, fungi, or other microorganisms, leading to alveolar filling with inflammatory exudates. Imaging shows localized or patchy consolidation with irregular margins, often accompanied by air bronchograms, pleural reaction, and mild pleural effusion. Clinically, patients present with fever, cough, sputum production, chest pain, and fatigue, with elevated white blood cell counts and inflammatory markers.
Consolidation	Consolidation refers to the complete filling of alveolar spaces with liquid, pus, blood, or cellular material, replacing the normal air content. Imaging shows homogeneous, dense, well-defined opacities, often with air bronchograms and pleural reactions, sometimes with minimal pleural effusion. Clinically, patients often have fever, cough, sputum production, chest pain, and dyspnea, with significantly elevated inflammatory markers.

864
865
866
867
868
869
870
871
872
873
874
875
876
877
878
879
880
881
882
883
884
885
886
887
888
889
890
891
892
893
894
895
896
897
898
899
900
901
902
903
904
905
906
907
908
909
910
911
912
913
914
915
916
917

918
919
920
921
922
923
924
925
926
927
928
929
930
931
932
933
934
935
936
937
938
939
940
941
942
943
944
945
946
947
948
949
950
951
952
953
954
955
956
957
958
959
960
961
962
963
964
965
966
967
968
969
970
971 Table 7: Semantic Descriptions of 75 Medical Categories

Disease	Description
normal	Indicates that the structure appears within standard parameters without signs of pathology.
clear	The imaging reveals no obscuring abnormalities, ensuring clear visualization of the structure.
sharp	Boundaries are precisely defined, accentuating the distinct separation between tissues.
sharply	The structure is rendered with exceptional clarity, facilitating detailed evaluation.
unremarkable	No significant deviations or abnormalities are observed in the examined area.
intact	The structure remains whole and undamaged, with no disruption detected.
stable	The tissue exhibits consistent appearance over time without progressive changes.
free	Presence of extraluminal air in unexpected locations, possibly indicating a perforation.
effusion	Accumulation of fluid between the pleural layers, often reflecting an underlying pathology.
opacity	An area of increased radiodensity that obscures normal lung markings, suggesting fluid or tissue replacement.
pneumothorax	Air present in the pleural space that may lead to partial or complete lung collapse.
edema	Diffuse fluid accumulation within lung tissue, frequently associated with cardiac or inflammatory issues.
atelectasis	Collapse of lung segments resulting in volume loss and increased local density.
tube	A medical tube visible on imaging, such as for drainage or airway management.
consolidation	Region where alveolar air is replaced by fluid or cells, producing homogeneous density.
process	Denotes an active pathological condition altering the tissue's normal appearance.
abnormality	A generic term for any deviation from normal structure suggestive of disease.
enlarge	Indicates that a structure appears larger than typical normal values.
tip	The distal or pointed end of a structure or medical device.
low	Underinflation of the lungs, often implying a restrictive process.
pneumonia	Inflammatory infection of lung parenchyma, typically showing consolidation and air bronchograms.
line	A linear structure that may represent a fissure, pleural interface, or artifact.
congestion	Increased blood or fluid accumulation in tissues, often indicating impaired circulation.
catheter	A slender, flexible tube inserted for drainage or medication delivery, visible in imaging.
cardiomegaly	An enlarged cardiac silhouette, frequently associated with chronic heart conditions.
fracture	A break or discontinuity in bone structure evident on radiographs.
air	Regions of radiolucency indicating the presence of gaseous content.
tortuous	Describes a vessel or structure exhibiting excessive curvature or winding.
lead	The foremost or guiding portion of a device or anatomical feature.
disease	A general term for any pathological process affecting normal tissue function.

972 Table 7: Semantic Descriptions of 75 Medical Categories
973

974 Disease	975 Description
976 calcification	975 Deposition of calcium salts within tissue, appearing as bright foci on imaging.
977 prominence	976 An area that appears more pronounced than surrounding tissues, suggesting an increase in size or density.
978 device	977 Any implanted or externally applied apparatus used for diagnostic or therapeutic purposes.
979 engorgement	978 Excessive filling of vessels or tissues with blood, leading to a swollen appearance.
980 picc	979 A long, thin catheter introduced via a peripheral vein and advanced into the central circulation for long-term therapy.
981 clip	980 A small metallic or plastic fastener used during surgery to secure tissues or vessels.
982 elevation	981 An upward displacement or raised position of an anatomical structure relative to its usual location.
983 expand	982 Describes a structure that appears dilated or increased in volume.
984 nodule	983 A small, rounded lesion typically less than 3 cm in diameter that can be benign or malignant.
985 wire	984 A thin, flexible metallic strand often used in surgical fixation or as part of medical devices.
986 fluid	985 The presence of liquid within tissues or cavities, altering the normal radiographic appearance.
987 degenerative	986 Changes in tissue structure resulting from chronic wear, aging, or repeated stress.
988 pacemaker	987 An implanted device that regulates heart rhythm, visible through its leads and generator.
989 thicken	988 Describes a structure that appears denser or more layered, possibly due to fibrotic changes.
990 marking	989 Visible patterns or lines that may represent vascular or connective tissue features.
991 scar	990 Fibrotic tissue that replaces normal parenchyma following injury, typically seen as an irregular opacity.
992 hyperinflate	991 Denotes lungs that are over-expanded, often with increased radiolucency and flattened diaphragms.
993 blunt	992 Loss of sharp definition in anatomical borders, leading to a less distinct appearance.
994 loss	993 Indicates a reduction or absence of normal tissue volume or density.
995 widen	994 Suggests that a structure or space is broader than the standard measurement.
996 collapse	995 A significant reduction or complete loss of volume in lung tissue due to obstruction or injury.
997 density	996 Reflects the compactness of a tissue, with higher density appearing whiter on radiographs.
998 emphysema	997 A chronic condition marked by alveolar wall destruction and abnormal enlargement of air spaces.
999 aerate	998 Indicates that the lung tissue is adequately filled with air, supporting effective gas exchange.
1000 mass	1000 A malignant tumor arising from lung tissue, typically presenting as an irregular mass with possible cavitation.
1001 crowd	1001 Compaction of airways and vessels, often due to volume loss or infiltrative processes.
1002 infiltrate	1002 Diffuse or patchy opacities in the lung that suggest inflammation, infection, or neoplastic involvement.
1003 obscure	1003 Describes anatomical structures that are not clearly visualized, often due to overlapping tissues or technical factors.

Table 7: Semantic Descriptions of 75 Medical Categories

Disease	Description
deformity	An abnormal shape or structure resulting from congenital anomalies, trauma, or disease progression.
hernia	The protrusion of an organ or tissue through an abnormal opening in the surrounding structure.
drainage	The process or presence of fluid removal from a body cavity, often via an inserted tube.
distention	Abnormal expansion or swelling of a structure due to accumulation of fluid or gas.
shift	Displacement of anatomical structures from their usual positions, indicating mass effect or volume change.
stent	A small mesh tube used to maintain the patency of a vessel or duct.
pressure	The force exerted per unit area by fluids or tissues, which can influence organ function.
lesion	Any abnormal area of tissue that deviates from the standard architecture, potentially indicative of pathology.
finding	A generic term for an observed abnormality or noteworthy feature on imaging.
borderline	The heart appears at the upper limit of normal size, without clear evidence of enlargement.
hardware	Any implanted or externally attached device used for diagnostic, therapeutic, or supportive purposes.
dilation	The widening or expansion of a hollow structure, often reflecting increased internal pressure.
chf	A clinical syndrome characterized by the heart's reduced pumping ability, leading to systemic fluid accumulation.
redistribution	A shift in the normal pattern of blood or air distribution within the lungs, often due to altered hemodynamics.
aspiration	Inhalation of foreign material into the airways, potentially leading to inflammatory or infectious complications.
rare diseases	Conditions that occur infrequently in the population and often require specialized diagnostic and management approaches.
Covid-19	An infectious disease caused by the SARS-CoV-2 virus, with a broad spectrum of respiratory and systemic manifestations.

1026
1027
1028
1029
1030
1031
1032
1033
1034
1035
1036
1037
1038
1039
1040
1041
1042
1043
1044
1045
1046
1047
1048
1049
1050
1051
1052
1053
1054
1055
1056
1057
1058
1059
1060
1061
1062
1063
1064
1065
1066
1067
1068
1069
1070
1071
1072
1073
1074
1075
1076
1077
1078
1079